Chapter 4

Enhanced convection and fast plumes in the lower mantle induced by the spin transition in ferropericlase

Originally published in:

Bower, D. J., M. Gurnis, J. M. Jackson, and W. Sturhahn (2009), Enhanced convection and fast plumes in the lower mantle induced by the spin transition in ferropericlase, *Geophys. Res. Lett.*, *36*, L10306, doi:10.1029/2009GL037706.

4.1 Abstract

Using a numerical model we explore the consequences of the intrinsic density change ($\Delta\rho/\rho \approx$ 2–4%) caused by the Fe^{2+} spin transition in ferropericlase on the style and vigor of mantle convection. The effective Clapeyron slope of the transition from high to low spin is strongly positive in pressure-temperature space and the transition broadens with high temperature. This introduces a net spin-state driving density difference for both upwellings and downwellings. In 2-D cylindrical geometry, spin-buoyancy dominantly enhances the positive thermal buoyancy of plumes. Although

the additional buoyancy does not fundamentally alter large-scale dynamics, the Nusselt number increases by 5–10%, and vertical velocities increase by 10–40% in the lower mantle. Advective heat transport is more effective and temperatures in the core-mantle boundary region are reduced by up to 12%. Our findings are relevant to the stability of lowermost mantle structures.

4.2 Introduction

A high-spin (four unpaired d electrons) to low-spin (no unpaired d electrons) electronic transition of divalent iron occurs in ferropericlase (Fp), a major lower mantle constituent, at around 50 GPa and 300 K (e.g., *Badro et al.* (2003); *Lin and Tsuchiya* (2008); *Lin et al.* (2007)). The transformation softens the elastic moduli over the transition pressure range (*Lin et al.*, 2006; *Crowhurst et al.*, 2008). *Auzende et al.* (2008) showed that the partition coefficient of iron between Fp and (Fe,Mg)SiO_3 perovskite (Pv) increases, although other experiments have shown little to no effect (*Sinmyo et al.*, 2008). These results have implications for mantle dynamics and seismic interpretation.

Theoretical (*Hofmeister*, 1999) and experimental (*Badro et al.*, 2003, 2004) studies partly motivate geodynamic simulations incorporating increases in radiative thermal conductivity and viscosity (*Matyska and Yuen*, 2005, 2006; *Naliboff and Kellogg*, 2006). However, contradictory high (*Hofmeister*, 2008; *Keppler et al.*, 2008) and low (*Goncharov et al.*, 2008) radiative conductivities need to be reconciled. Arguably, the most well-defined effect of the spin transition in pyrolite-like Fp is a 2–4% density

increase from the high to low spin state at 300 K (*Sturhahn et al.*, 2005; *Lin and Tsuchiya*, 2008; *Fei et al.*, 2007), yet the influence on mantle flow has yet to be determined. The continuous nature of the spin transition along a lower mantle geotherm (*Sturhahn et al.*, 2005; *Tsuchiya et al.*, 2006) has presumably discouraged such studies. Downwellings and upwellings may generate substantial temperature anomalies in the mantle, so that convective flow may be modified by buoyancy forces arising through the spin-state of the material.

4.3 Numerical models

4.3.1 Spin buoyancy formulation

We modify version 3.0 of the finite element code CitcomS (*Zhong et al.*, 2000; *Tan et al.*, 2007) to solve the equations for the conservation of mass, momentum, and energy for incompressible flow. We incorporate a spin-buoyancy body force similiar to a phase function formulation (*Richter*, 1973; *Christensen and Yuen*, 1985). We found that the spin function as determined from a theoretical temperature- and pressure-dependent spin-state model cannot be accurately represented analytically. We therefore pre-compute the spin-state model as a function of temperature for each pressure defined by the radial meshing. Stored as a look-up table, the code accesses and interpolates the data at each time step to determine the spin-state function. The additional body force term is equal to the spin-state function multiplied by a spin Rayleigh number. Since latent heat is a non-Boussinesq effect (*Christensen and Yuen*,

1985), the entropy changes associated with the spin transition are not included in the energy equation. In previous studies, latent heat has been found to be of secondary importance in mantle phase transitions (*Olson and Yuen*, 1982).

We select the $(Mg_{83}Fe_{17})O$ spin-state model (*Sturhahn et al.*, 2005), except that the model is translated by -10 GPa in accordance with recent experimental results showing that the transition at 300 K occurs at about 50 GPa (see *Lin and Tsuchiya* (2008) for a review). We non-dimensionalize by a surface temperature, $T_0 = 300$ K, temperature drop, $\Delta T = 2700$ K, and a pressure scale of 40 MPa/km. For this particular model, the high-low spin density contrast is reported to be 2.3%, consistent with high-pressure x-ray diffraction studies (*Lin and Tsuchiya*, 2008).

4.3.2 Model setup

We develop a suite of models with the Boussinesq approximation within a 2-D section (1 radian). The mesh size is 257 x 129 nodes with refinement in the radial direction within the boundary layers. Isothermal and free-slip boundary conditions are imposed at the top and bottom boundaries and the two sidewalls have a zero heat flux boundary condition.

Viscosity is computed by a temperature-dependent linearized Arrhenius law, $\eta(T) = \eta_0 \exp(A(0.5 - T))$, where $\eta_0 = 1$ for the upper mantle, 10 for the transition zone, and 30 for the lithosphere and lower mantle. The reference value is 10^{21} Pa·s at $T = 0.5$. The activation energy, A, and thermal and spin Rayleigh number, Ra are free parameters (Table 4.1). Ra spans a range to contrast vigourous upper mantle

convection with sluggish lower mantle convection. To ensure mobile-lid convection, we use low activation energies so that the viscosity contrast is less than four orders of magnitude. The phase changes within the mantle are not included, so that the effect of the Fe^{2+} spin transition is isolated. Internal heat sources are not considered.

4.3.3 Procedure

After integrating from a conductive temperature profile for 100,000 time steps (dimensionally several Ga) the system has a reached statistical steady state, as evident through small oscillations of the top and bottom Nusselt numbers (Nu) and the laterally averaged temperature profile. Two models are then initialized from the final state: The first with the spin transition, and the second without. Both are integrated for a further 100,000 time steps. In addition to observing the pattern of convection, we apply three measures to determine the influence of the spin transition. At steady state, we compare time-averaged top and bottom Nu's and depth profiles for the horizontally averaged temperature (reference geotherm) and RMS vertical velocity. We only report the top Nu because for most cases the Nu's differ by only a fraction of a percent (Table 4.1).

4.4 Results

The spin-state model reveals a strongly positive effective Clapeyron slope (Fig. 4.1d). Relative to the reference geotherm, this generates buoyancy by transforming cold (warm) material to the more- (less-) dense phase at a lower (higher) pressure. The

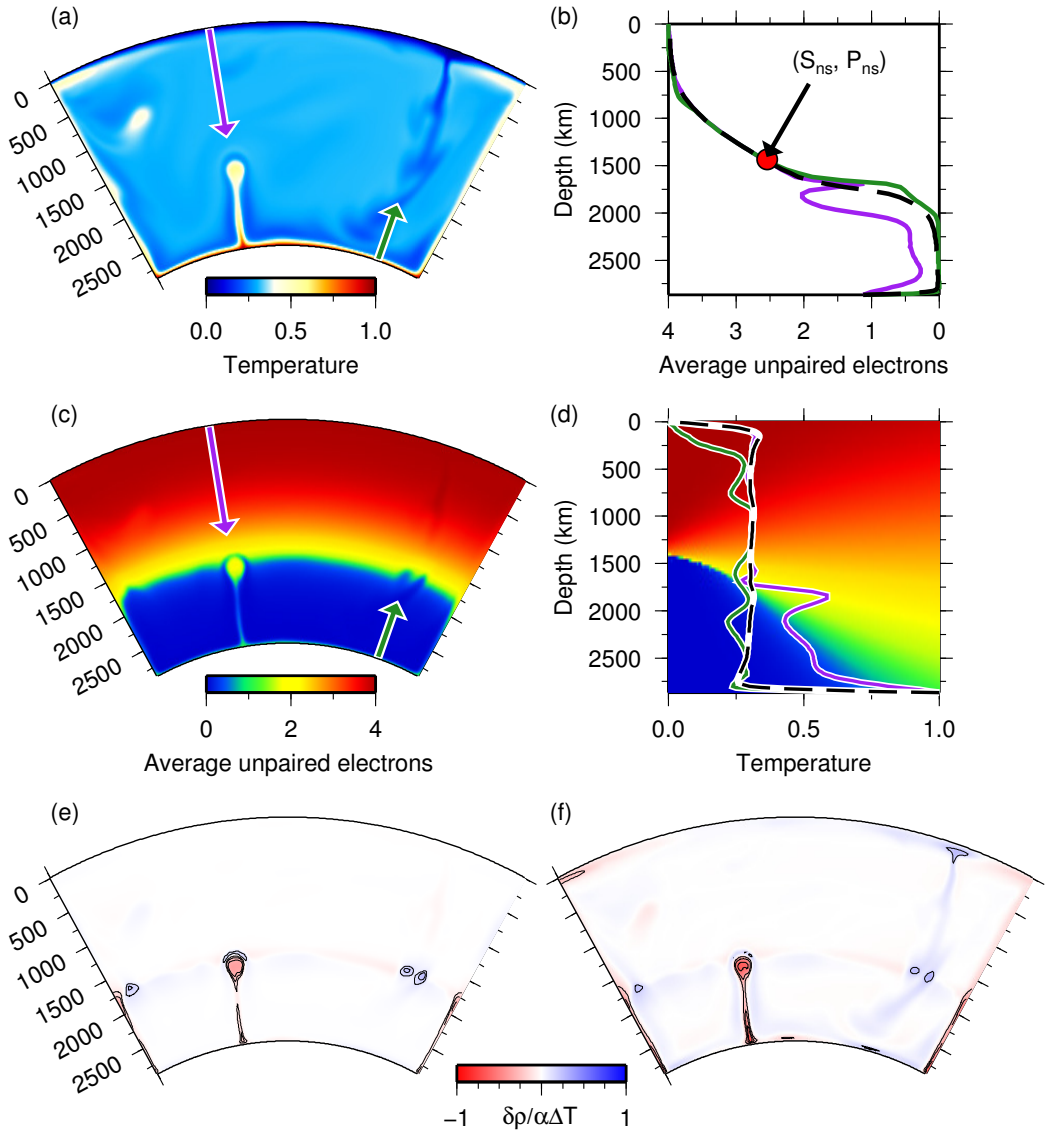

Figure 4.1: Snapshot from Case 13 at quasi-steady state. (a) Non-dimensional temperature. The purple and green lines delineate the location of representative warm and cold geotherms respectively, referred to in subsequent panels. (b) Unpaired electrons (spin-state) for representative warm (purple) and cold (green) geotherms. Red dot is (S_{ns},P_{ns}) for the spin-state model (see text). Black dashed line is the reference (horizontally averaged) spin-state. (c) Unpaired electrons with geotherm locations. (d) Geotherms with *Sturhahn et al.* (2005) spin-state model. Black dashed line is the reference geotherm. (e) Spin density anomaly, scaled by $1/\alpha\Delta T$, relative to the horizontally averaged profile. Contour interval is 0.1. (f) Total density anomaly, scaled by $1/\alpha\Delta T$, relative to the horizontally averaged profile. Contour interval is 0.2.

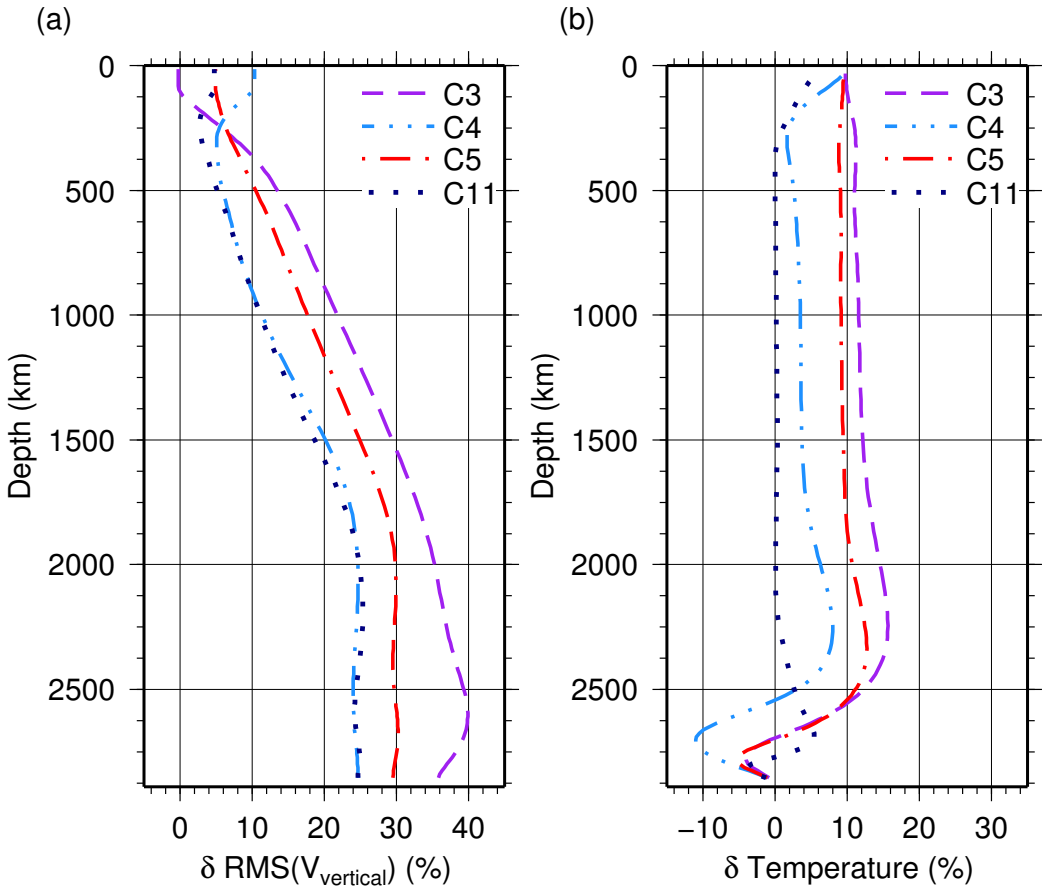

Figure 4.2: Fractional change (horizontally averaged) caused by the spin transition (%) for representative cases at quasi-steady state. (a) RMS vertical velocity. (b) Temperature

temperature broadening envelope causes cold (warm) material to transform within a tight (broad) pressure range. This introduces a neutral spin-buoyancy pressure (P_{ns}) at which the spin-state (S_{ns}), biased toward high-spin, is independent of temperature (Fig. 4.1b). This arises through the approximately temperature-independent spin contour at P_{ns}, and explains the common intersection point for the representative geotherms.

Table 4.1: Input and output characteristics of the models. Ra is the Rayleigh number, A is the activation energy, and regime indicates the style of convection. Nu is the Nusselt number and Vz is the vertical velocity at 2500 km depth. "n" and "s" subscripts denote models without and with the spin transition, respectively. A standard deviation is given for the time-dependent cases. ΔNu and ΔVz are the change in the Nusselt number and vertical velocity due to the spin transition.

Case	Input		Output						
	Ra	A	Regime	Nu_n	Nu_s	ΔNu(%)	Vz_n	Vz_s	ΔVz (%)
1	5×10^6	0	Steady	11.40	12.47	9.4	338.0	419.3	24.1
2	5×10^6	4	Steady	9.52	10.43	9.5	256.3	334.8	30.6
3	5×10^6	6	Steady	8.79	9.64	9.7	240.1	334.7	39.4
4	1×10^7	0	Steady	11.51	12.65	9.9	404.6	501.7	24.0
5	1×10^7	4	Steady	11.56	12.66	9.5	384.2	498.3	29.7
6	1×10^7	6	Steady	10.54	11.57	9.9	358.4	496.3	38.5
7	5×10^7	0	Steady	19.47	21.15	8.6	1178.5	1436.2	21.9
8	5×10^7	4	Time-dependent	18.11±0.11	19.10±0.22	5.5	959.2±15.2	1195.7±59.3	24.7
9	5×10^7	6	Time-dependent	13.10±0.61	14.13±0.62	7.9	569.4±116.9	737.7±204.9	29.6
10	1×10^8	0	Time-dependent	24.39±0.03	26.13±0.43	7.1	1702.5±2.4	2091.6±88.4	22.9
11	1×10^8	4	Time-dependent	21.37±0.49	22.67±0.41	6.1	1373.1±84.0	1707.4±115.3	24.0
12	1×10^8	6	Time-dependent	16.56±0.64	17.37±1.26	4.9	864.4±200.4	1061.2±223.1	22.8
13	5×10^8	4	Time-dependent	30.55±2.35	31.80±2.33	4.1	2981.8±639.9	3276.3±683.8	9.9

The spin transition increases vertical velocities throughout the mantle (Fig. 4.2a) with 10-40% increases in the lowermost mantle, tapering to near zero at the surface. Temperatures in the interior of the mantle are raised by up to 12%, except for the region above the core-mantle boundary (CMB) where they are reduced by an average of 5% (Fig. 4.2b). For both of these profiles, the percentage increase is inversely proportional to Ra and scales with A. The Nusselt number increases between 4 and 10% (Table 4.1) and scales inversely with Ra.

High temperatures within the lower thermal boundary layer (Figs. 4.1a and 4.1d) cause instabilities to develop with a bias toward high spin-state (Fig. 4.1c). At depth, these upwellings have both positive thermal and spin buoyancy that generates higher advective velocities (Fig. 4.2a). This increases the rate of heat removal, consistent with the reduced temperatures above the CMB in our models (Fig. 4.2b). Driving spin-state density differences in upwellings are distributed over a broad pressure range (Fig. 4.1e). As material passes through P_{ns}, the spin-buoyancy changes from working with thermal buoyancy to mildly opposing it (Fig. 4.1b). Thermal forcing continues to drive upward advection (Fig. 4.1f), albeit at a reduced velocity. Downwellings are less affected by the spin transition as the net change in buoyancy about P_{ns} is negligible because of smaller temperature differences between cold and ambient material than for warm, particularly at high pressure (Fig. 4.1d). This is controlled, in part, by the cylindrical geometry, rheological law, and pure basal heating. Driving spin-state density differences within downwellings are constrained within a comparatively tight pressure range (Fig. 4.1e). Positive spin-state buoyancy at pressures less

than P_{ns} slightly retards downward advection, but at greater pressures spin-buoyancy mildly enhances downward motion. Therefore, both upwellings and downwellings are impeded by spin-buoyancy at pressures less than P_{ns} and are enhanced at pressures greater than P_{ns}. The asymmetry ($S_{ns} < 2$) of the spin-state model ensures that a net force exists in both cases.

4.5 Discussion and conclusions

The dominant effect of buoyancy caused by the spin transition is comparable to a strongly exothermic phase change, similar to a discrete phase change (*Christensen and Yuen*, 1985). However, the nature of the Fe^{2+} spin transition generates buoyancy over a broader pressure range for upwellings than for downwellings. Spin-forcing depends strongly on temperature contrasts, with our models predicting increased plume velocities and heat transfer, and marginally reduced temperatures above the CMB. The temperature-broadening of the transition precludes significant perturbation to the bulk Earth 1-D velocity profile (*Masters*, 2008). Seismic detection will require a focus on cold slabs where the transition occurs abruptly with the potential for a seismic discontinuity. A detailed mapping of localized structures to observed seismic velocities requires more accurate knowledge of the high P-T wave speeds in candidate phase assemblages.

The spin transition, in addition to the Pv-pPv phase change, is a destabilizing mechanism in the lowermost mantle that will further work against the stability of high-density (*McNamara and Zhong*, 2005) or high-bulk modulus (*Tan and Gurnis*,

2005) structures. Furthermore, it provides additional buoyancy to small-scale hot plumes, such as those that possibly emanate from the edges of large, low-velocity structures (*Sun et al.*, 2009a). Transient systems with non-Newtonian rheology and 3-D geometry may behave differently. Additionally, iron concentration in Fp affects the transition pressure (e.g., *Fei et al.*, 2007), and iron-enriched upwellings and depleted downwellings may have different spin-state models.